UNIVERSITY OF LEEDS

This is a repository copy of *Dynamics of high-speed rail ballasted tracks on asphaltic support layers*.

White Rose Research Online URL for this paper:
https://eprints.whiterose.ac.uk/id/eprint/235525/

Version: Accepted Version

Article:

Wang, T., Lin, L., Yan, Z. et al. (3 more authors) (2025) Dynamics of high-speed rail ballasted tracks on asphaltic support layers. Construction and Building Materials, 494. 143382. ISSN: 0950-0618

https://doi.org/10.1016/j.conbuildmat.2025.143382

This is an author produced version of an article published in Construction and Building Materials, made available under the terms of the Creative Commons Attribution License (CC-BY), which permits unrestricted use, distribution and reproduction in any medium, provided the original work is properly cited.

Reuse

This article is distributed under the terms of the Creative Commons Attribution (CC BY) licence. This licence allows you to distribute, remix, tweak, and build upon the work, even commercially, as long as you credit the authors for the original work. More information and the full terms of the licence here: https://creativecommons.org/licenses/

Takedown

If you consider content in White Rose Research Online to be in breach of UK law, please notify us by emailing eprints@whiterose.ac.uk including the URL of the record and the reason for the withdrawal request.

White Rose
university consortium
Universities of Leeds, Sheffield & York

eprints@whiterose.ac.uk
https://eprints.whiterose.ac.uk/

Dynamics of Ballasted High-Speed Railway Tracks on Asphaltic Support Layers

Tengfei Wang [1], Liting Lin [1], Zhongcheng Yan [1], David P. Connolly [2], Qiang Luo [1], Kaiwen Liu [1,*]

1. Key Laboratory of High-Speed Railway Engineering (Ministry of Education), School of Civil Engineering, Southwest Jiaotong University, Chengdu 610031, China
2. School of Civil Engineering, University of Leeds, Leeds LS2 9JT, UK

* Corresponding author: kaiwen.liu@queensu.ca (K. Liu)

Abstract

With the continued expansion of high-speed railway (HSR) networks, trackbeds must withstand ever-increasing cyclic loads without compromising safety or serviceability. This study quantifies the dynamic and long-term performance benefits of incorporating asphaltic support layers (ASLs) beneath conventional ballast. To do so, a two-stage hybrid model is developed: (1) a MATLAB-based vehicle–track interaction model that yields wheel–rail forces in the presence of measured track irregularities, and, (2) a 3D finite element (FE) substructure model that calculates stresses, displacements, and accelerations throughout the ballast–subgrade system, where asphalt is modelling using a Prony series approach. Field data from the Beijing–Zhangjiakou HSR line is used to validate the model, with simulated stress and vibration amplitudes showing close correlation with the field measurements. Parametric studies show that a 10 cm ASL lowers peak dynamic stresses in the subgrade by ≈55% yet leaves net vertical deflection virtually unchanged. Increasing ASL thickness from 8 cm to 15 cm further attenuates subgrade stresses, while a 30°C rise in ambient temperature cuts stress-reduction efficiency by ≈25%. Fatigue and permanent-deformation analyses demonstrate that all tested thicknesses satisfy a 100-year design life, and stability checks confirm that subgrade reaction moduli comfortably exceed thresholds commonly used in international standards. A 10 cm ASL therefore offers a balance between asphalt material cost and performance enhancement.

Keywords: high-speed railway; ballasted-aspahlt track; asphaltic support layer; Prony series; railway dynamic response; finite element

1. Introduction

With the rapid expansion and operation of high-speed railway (HSR) networks globally, maintaining stable and reliable railway substructures under dynamic train loading has become increasingly important. In contrast to traditional railway lines, HSRs must adhere to stricter track geometry tolerances and thus issues such as differential settlement, ballast degradation and subgrade deterioration [1,2] must be carefully controlled.

In conventional ballasted railway track systems, the rails and sleepers directly rest upon a ballast layer that provides structural support, drainage and load distribution. However, prolonged exposure to repetitive train loads can lead to ballast degradation, particle crushing, settlement and poor drainage ability, subsequently diminishing the functionality of the ballast layer [2,3]. To mitigate these issues, asphaltic support layers (ASLs) beneath ballast layers have increasingly been adopted internationally due to their potential benefits such as enhancing mechanical behaviour, providing waterproofing [4–6] and also providing a working platform during track construction. Asphalt mixtures are characterized by desirable viscoelastic properties and impermeability, which can prevent water infiltration, reduce particle degradation, and offer improved vibration damping [6]. Early implementation of asphaltic materials in railway track structures dates back to the 1960s, notably in countries like the United States, Japan, Italy, and Austria, indicating their long-standing reliability in diverse railway environments [7-8].

International practices demonstrate various methodologies for incorporating asphalt into track structures. The United States primarily utilizes asphalt layers ranging from 0.125 to 0.15 m thick beneath the ballast [7-8], whereas European nations such as France, Italy, and Spain typically adopt asphalt layer thicknesses between 0.12 and 0.14 m [9–13]. In Japan, thinner asphalt layers of approximately 0.05 m are implemented in combination with graded crushed stone layers to strengthen existing track foundations, yielding reduced lateral and vertical strains compared to traditional ballast designs. Within China, recently constructed lines such as the Beijing-Zhangjiakou high-speed railway, have employed asphaltic support layers with a thickness around 0.10 m, due to the perceived benefits related to structural rigidity and serviceability under dynamic loads [14,15].

Despite extensive international experience and demonstrated advantages, existing research predominantly focuses on slab track systems, leaving a notable research gap regarding the application of asphaltic support layers in ballasted track configurations. Moreover, earlier studies often simplified dynamic train-track interactions to moving point loads, neglecting realistic scenarios involving track irregularities and vehicle-track coupling, thus limiting the practical applicability of the results [2]. Furthermore, dynamic responses at critical locations, including longitudinal track discontinuities and interfaces between different layers, have typically been overlooked, despite their significant implications for track design and maintenance.

Addressing these knowledge gaps, this paper investigates the dynamic behavior of ballasted railway tracks incorporating asphaltic support layers under realistic train-track interaction conditions. The research uses a hybrid modeling approach combining a coupled vehicle-track dynamics model and a refined three-dimensional finite element (FE) substructure model. This integrated methodology allows for the characterization of track dynamic response, stress propagation and deformation under typical operating conditions.

The objectives of this study are threefold: firstly, to validate the developed numerical model through comparison with field measurements from existing ballasted track sections incorporating asphaltic layers; secondly, to analyze the influence of asphaltic support layer thickness and mechanical properties on dynamic responses, including track deflections, accelerations, stresses, and strains; and finally, to assess the durability and long-term stability of asphaltic support layers under continuous high-speed operations and varying environmental conditions.

By addressing these aspects, the study aims to enhance understanding of the structural benefits and performance characteristics of asphaltic support layers within ballasted tracks. It also aims to provide insights and guidelines for optimizing the design, implementation, and maintenance of asphaltic layers in high-speed railway ballasted track structures, contributing to the improved reliability and longevity of railway infrastructure worldwide.

2. Modeling Framework

Train-induced vibrations in a ballasted track arise primarily from wheel and rail surface unevenness. To capture these effects and the influence of an asphalt layer in the track foundation, a hybrid two-step modeling approach is adopted.

2.1. Integrated modeling methodology

In the first step, a vehicle–track coupled dynamics model computes the time-varying wheel–rail forces under realistic track irregularities. In the second step, a three-dimensional (3D) finite element (FE) substructure model uses those forces as input to evaluate the detailed response of the track’s supporting layers (including ballast and asphaltic sublayers). Both sub-models operate in the time domain and are synchronized such that the output of the first provides the loading conditions for the second. Figure

1 illustrates the overall approach, which can be summarized as follows:

1) **Vehicle–Track Dynamics Sub-Model:** A train–track interaction model is developed in MATLAB to calculate the vertical wheel–rail contact forces under a moving vehicle. The vehicle is represented as a multi-body system with sprung and unsprung masses and suspension elements, while the track is represented by an infinite rail supported on a foundation that includes the sleeper, ballast, and ASL-improved subgrade. These subsystems are coupled through the wheel–rail contact interface using a nonlinear Hertzian spring. Random track irregularities serve as the excitation input to this model, leading to dynamic wheel loads that vary over time and space.

2) **Track–Substructure FE Sub-Model:** A detailed 3D FE model of the track substructure (built in ABAQUS) is used to simulate the ground and structural response under the dynamic loads obtained from Step 1. This model includes the rails, sleepers, ballast, asphalt layer, and underlying subgrade, allowing for realistic representation of material behavior (e.g. elasticity or viscoelasticity of asphalt), geometric layering, and boundary conditions. The time-history of wheel–rail forces from the vehicle–track model is applied to the FE model (as time-dependent forces on the rails/sleepers) to compute the resulting stresses, strains, and displacements in the track foundation. Appropriate non-reflective boundary conditions are implemented to absorb outward-propagating waves at the model edges, ensuring the FE domain behaves like an infinite track-ground system.

This integrated methodology leverages the strengths of both models: the vehicle–track dynamics sub-model efficiently captures high-frequency vehicle interactions and wheel load fluctuations, while the 3D FE sub-model provides rigorous insight into the performance of the ballast and ASLs under those loads. By coupling the two in the time domain, the approach accounts for speed-dependent dynamic effects and load histories, which is crucial for evaluating the impact of ASLs on track performance.

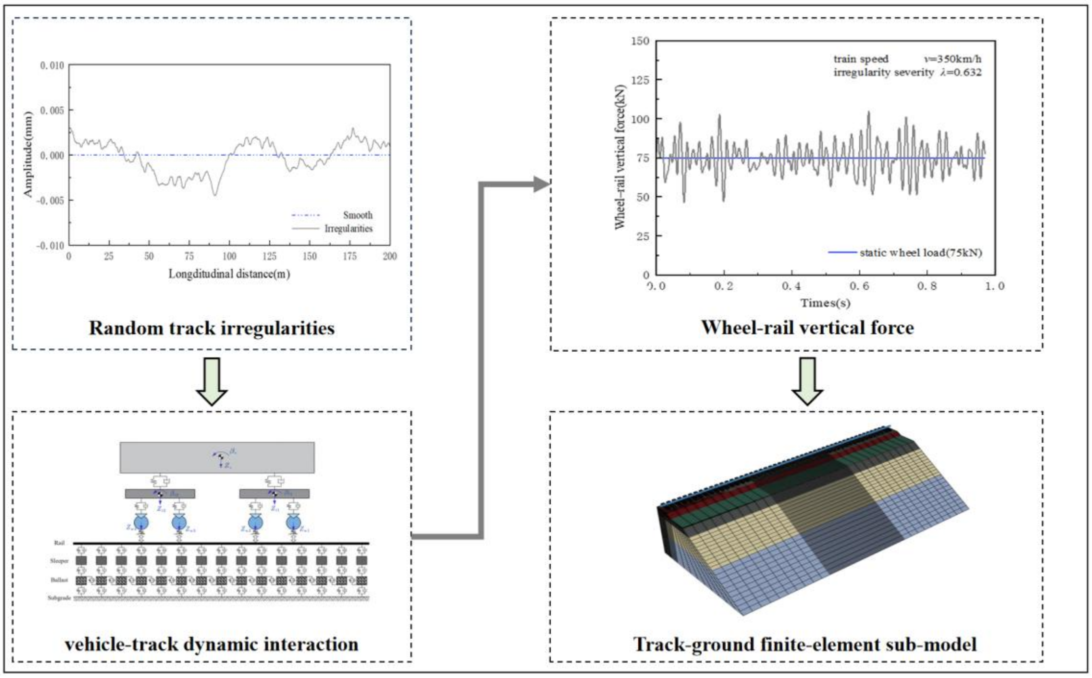

Figure 1. Schematic of the integrated two-stage modelling framework coupling vehicle–track dynamics and finite-element substructure analysis

2.2 Vehicle−track vertical coupled dynamics model

The vertical vehicle–track interaction is modeled using a coupled dynamics approach, in which the vehicle is simplified as a multi-body system and the track as a beam–discrete support structure. Higher-frequency phenomena such as wheel–rail noise are not considered and the rail is represented as an Euler–Bernoulli beam. To account for the localized vibration response at discrete sleeper supports and the contribution from ballast layers, a three-layer discretely supported beam model is employed (Figure 2).

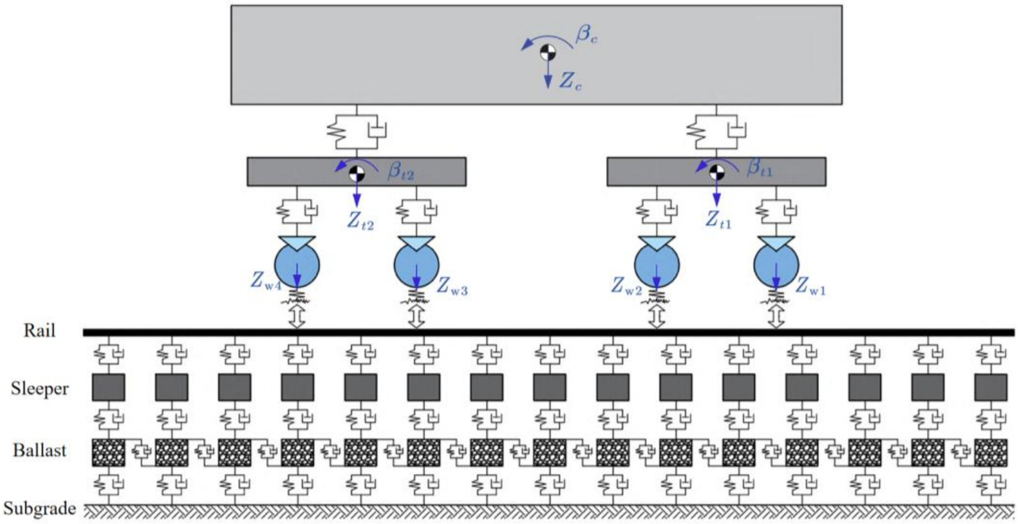

Figure 2. Cross-section of the vertical vehicle–track interaction sub-model with discrete subgrade supports

The governing dynamic equations of the coupled system are formulated and solved using MATLAB. The assembled equations of motion in matrix form are expressed as follows [16,17]:

$$\begin{bmatrix} \mathrm{M_v} & 0 \\ 0 & \mathrm{M_t} \end{bmatrix} \begin{pmatrix} \ddot{\mathrm{q}}_\mathrm{v} \\ \ddot{\mathrm{q}}_\mathrm{t} \end{pmatrix} + \begin{bmatrix} \mathrm{C_v} & 0 \\ 0 & \mathrm{C_t} \end{bmatrix} \begin{pmatrix} \dot{\mathrm{q}}_\mathrm{v} \\ \dot{\mathrm{q}}_\mathrm{t} \end{pmatrix} + \begin{bmatrix} \mathrm{K_v} & 0 \\ 0 & \mathrm{K_t} \end{bmatrix} \begin{pmatrix} \mathrm{q_v} \\ \mathrm{q_t} \end{pmatrix} = \begin{pmatrix} \mathrm{P_v} \\ \mathrm{P_t} \end{pmatrix} \tag{1}$$

where subscripts *v* and *t* denote vehicle and track, respectively.

The rail vibration is further governed by a differential equation based on Euler beam theory, discretized using the Ritz method:

$$EI_Y \frac{\partial^4 Z_\mathrm{r}(x,t)}{\partial x^4} + m_\mathrm{r} \frac{\partial^2 Z_\mathrm{r}(x,t)}{\partial t^2} = -\sum_{i=1}^{N} F_{\mathrm{rs}i}(t)\,\delta(x - x_i) + \sum_{j=1}^{4} P_j \delta(x - x_{\mathrm{w}j}) \tag{2}$$

where EI_Y is the rail bending stiffness, Z_r (x, t) is the rail deflection, m_r is the rail mass per unit length, *N* is the number of sleeper supports, and P_j is the wheel–rail contact forces. The rail displacement Z_r (x, t) is approximated using modal expansion:

$$Z_\mathrm{r}(x,t) = \sum_{k=1}^{NM} Z_k(x) q_k(t) \tag{3}$$

where *NM* represents the number of vibration modes considered.

For the sleeper and ballast layers discretized at each sleeper location, the vibration equations are:

$$M_{\mathrm{s}i}\ddot{Z}_{si}(t)+\left(C_{\mathrm{p}i}+C_{\mathrm{b}i}\right)\dot{Z}_{\mathrm{s}i}(t)+\left(K_{\mathrm{p}i}+K_{\mathrm{b}i}\right)Z_{\mathrm{s}i}(t)-C_{\mathrm{b}i}\dot{Z}_{\mathrm{b}i}(t)-K_{\mathrm{b}i}Z_{\mathrm{b}i}(t)$$

$$-C_{\mathrm{p}i}\sum_{h=1}^{NM}Z_h(x_i)\dot{q}_h(t)-K_{\mathrm{p}i}\sum_{h=1}^{NM}Z_h(x_i)q_h(t)=0\ \ (i=1\approx N) \tag{4}$$

$$M_{\mathrm{b}i}\ddot{Z}_{\mathrm{b}i}(t)+(C_{\mathrm{b}i}+C_{\mathrm{f}i}+2C_{\mathrm{w}i})\dot{Z}_{\mathrm{b}i}(t)+(K_{\mathrm{b}i}+K_{\mathrm{f}i}+2K_{\mathrm{w}i})Z_{\mathrm{b}i}(t)$$

$$-C_{\mathrm{b}i}\dot{Z}_{si}(t)-K_{\mathrm{b}i}Z_{\mathrm{s}i}(t)-C_{\mathrm{w}i}\dot{Z}_{\mathrm{b}(i+1)}(t)-K_{\mathrm{w}i}Z_{\mathrm{b}(i+1)}(t)$$

$$-C_{\mathrm{w}i}\dot{Z}_{\mathrm{b}(i+1)}(t)-K_{\mathrm{w}i}Z_{\mathrm{b}(i+1)}(t)=0\quad(i=1\approx N) \tag{5}$$

where M_{si}, M_{bi}, C_{pi}, K_{pi}, and C_{bi}, K_{bi}, C_{fi}, K_{fi}, C_{wi}, K_{wi} represent the mass, damping, and stiffness parameters for sleepers, ballast, and subgrade.

The vehicle–track interaction force is described using nonlinear Hertzian contact theory as follows:

$$P_j(t)=\begin{cases}\left\{\dfrac{1}{G}\left[Z_{\mathrm{w}j}(t)-Z_{\mathrm{r}}\left(x_{\mathrm{w}j},t\right)-Z_0(t)\right]\right\}\\ 0\ \ (\mathrm{Detached})\end{cases} \tag{6}$$

where G is the contact constant.

Random track irregularities are modeled using power spectral density (PSD) functions based on measured railway track profiles. These frequency-domain irregularities are transformed into time-domain samples via inverse Fourier transform, incorporating randomly generated phases through Monte Carlo simulations. A typical realization of vertical track irregularities is shown in Figure 3.

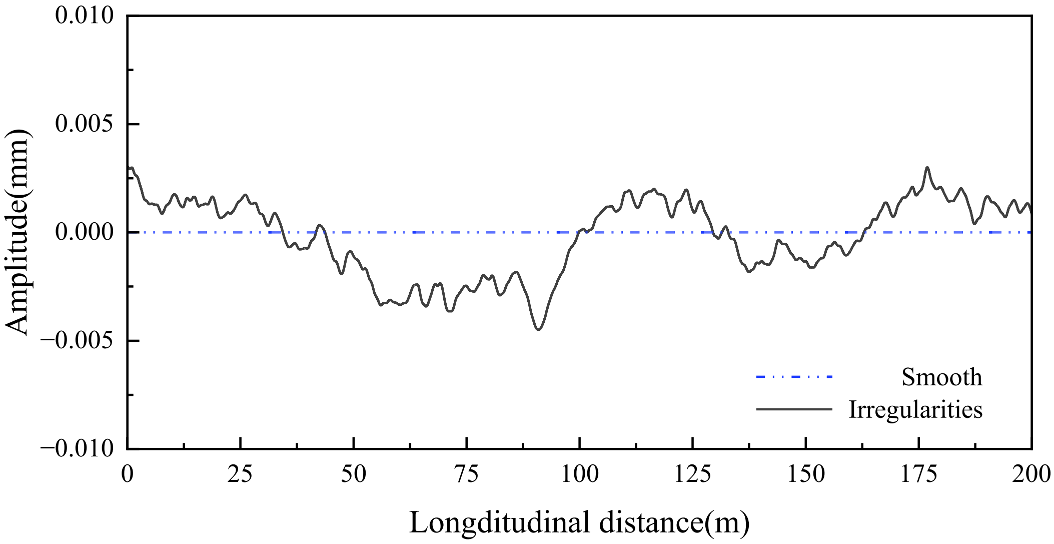

Figure 3. Representative track-irregularity profile at 350 km/h derived from measured power spectral density.

Considering vehicle speeds of 5, 300, and 350 km/h and irregularity levels characterized by cumulative probabilities (λ = 0.632 and λ = 0.99), computed wheel–rail vertical force time histories used for FE simulations are illustrated in Figure 4.

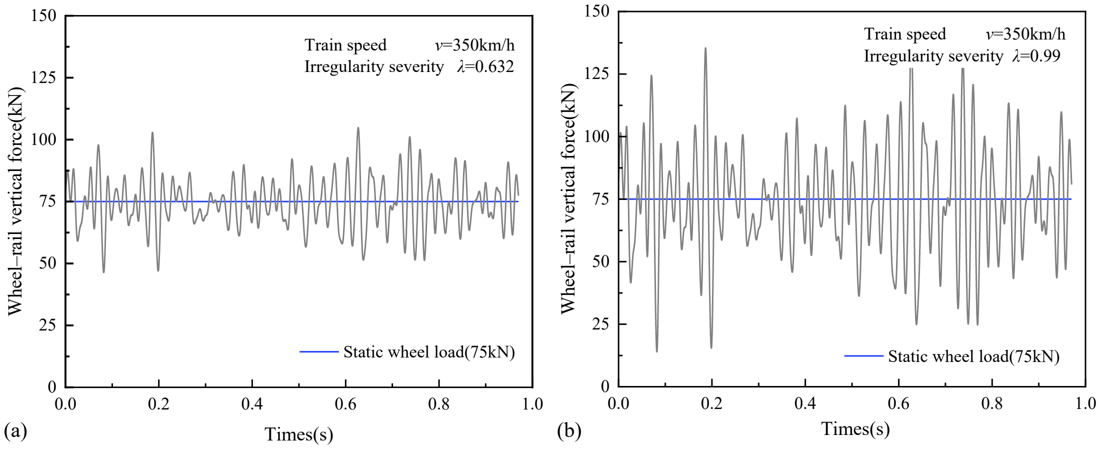

(a) (b)

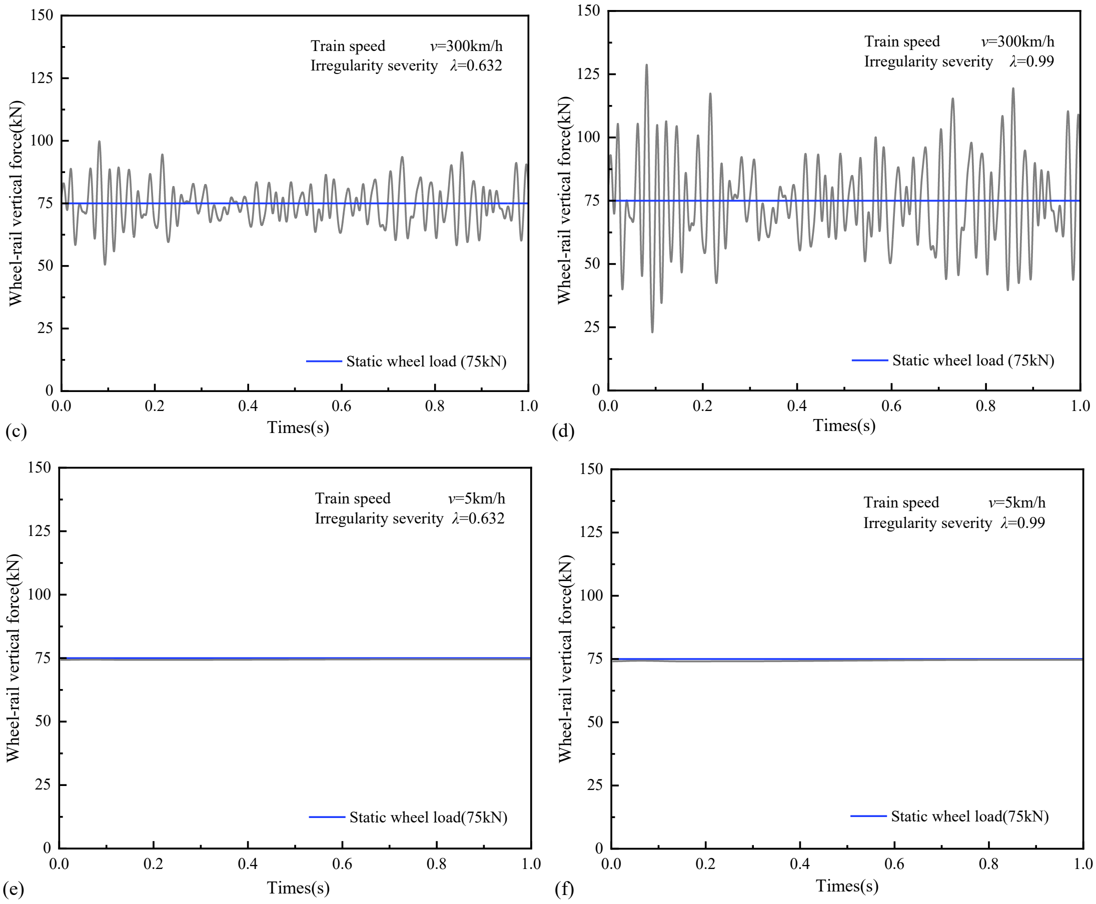

Figure 4. Wheel–rail vertical force histories for two train speeds (300 km/h and 350 km/h) and two irregularity severity levels (λ = 0.632 and 0.99). Panels (a)–(f) correspond to the combinations indicated.

2.3 Three-dimensional finite-element substructure model

To accurately analyze stresses and deformations within the track foundation under dynamic train loads, a three-dimensional FE model was constructed using ABAQUS. The modeled track structure includes standard UIC60 rails, concrete sleepers, a ballast layer, an ASL and underlying subgrade layers (Figure 5). The rails were represented using two-node elastic beam elements, enabling efficient modeling of rail bending while maintaining computational efficiency. Concrete sleepers, discretely placed at regular intervals (e.g. 0.6 m spacing), are modeled as solid elements connected to the rails through rail pad stiffness and damping properties defined using spring–damper connectors.

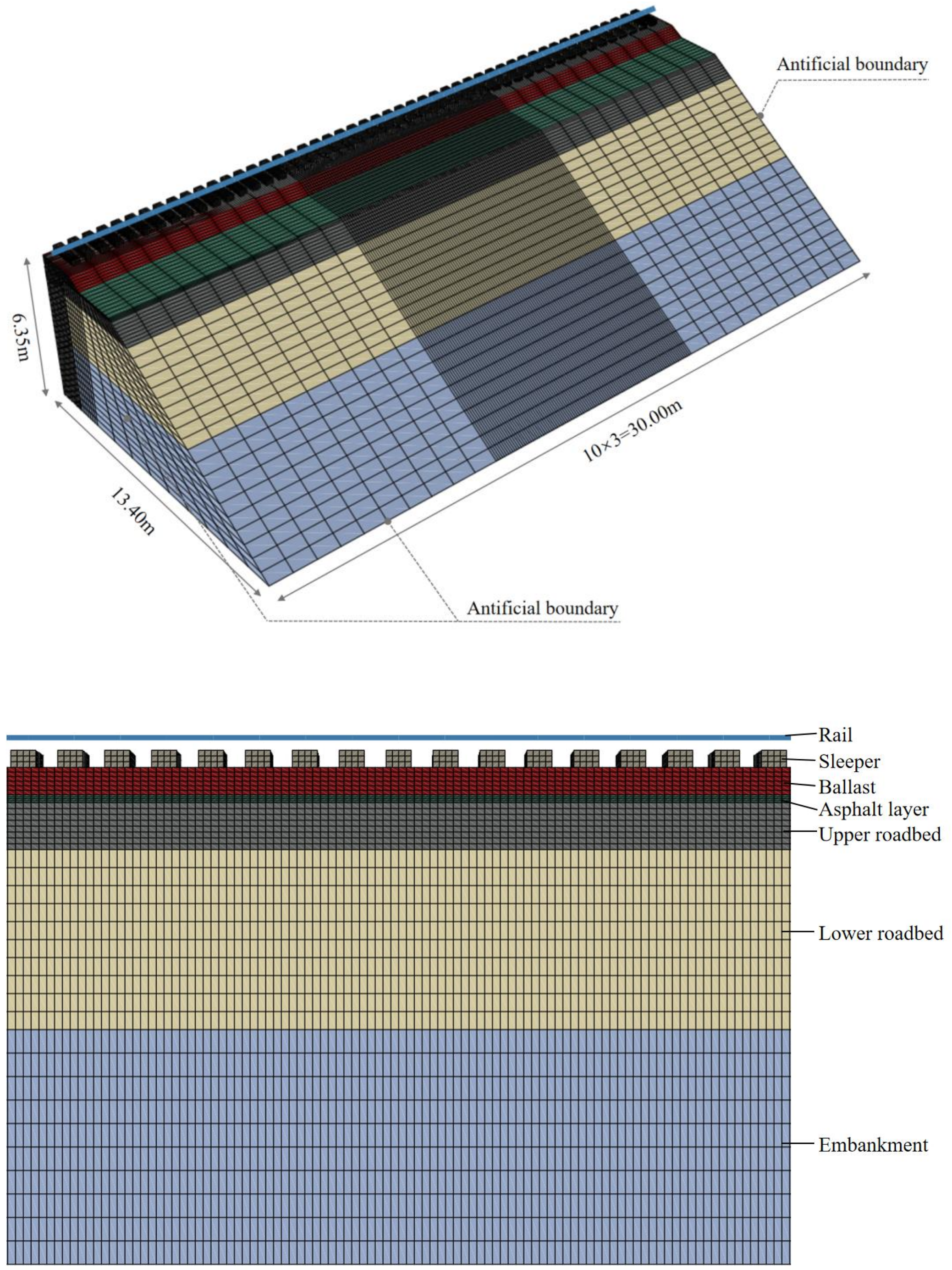

Figure 5. Overview of the three-dimensional track-substructure finite-element model: (a) general view; (b) elevation view.

Table 1 summarizes material densities, elastic moduli, Poisson's ratios, and Rayleigh damping coefficients for each modeled component. The ballast bed, approximately 0.3 m thick, is discretized using eight-node solid elements assigned linear elastic properties and damping representative of compacted granular material.

Table 1. Material properties adopted in the finite-element analysis.

Component	Density (kg/m³)	Elastic Modulus (MPa)	Poisson's Ratio	α (s^{-1})	β (s)
Rail	7830	210000	0.30	0.0328	0.0031
Sleeper	2300	36000	0.30	0.0984	0.0093
Ballast	1800	150	0.27	0.0656	0.0062
Asphalt Layer	2400	1600	0.30	0.0328	0.0031
Graded Gravel	2150	200	0.25	0.2624	0.0248
Subgrade Top	2050	130	0.25	0.2296	0.0217
Embankment	2000	160	0.25	0.3280	0.0310

Beneath the ballast, the ASL (approximately 0.1–0.15 m thick) is modeled as a viscoelastic solid layer, characterized using a Prony series calibrated to laboratory-derived frequency-dependent stiffness and damping properties [18] (Table 2). This viscoelastic formulation allows realistic representation of asphalt's temperature- and frequency-sensitive behavior under dynamic loading conditions. The temperature-dependent behavior of the asphalt is modeled using the Williams-Landel-Ferry equation for time–temperature superposition [19]:

$$\log \alpha_T = \log \frac{\tau}{\tau_r} = \frac{-C_1(T - T_r)}{C_2 + (T - T_r)} \tag{8}$$

where α_T is a shift factor, T is the actual temperature, and T_r is the reference temperature.

Table 2. Generalized Maxwell (Prony series) model parameters calibrated from laboratory tests at 20 °C.

Term	Relaxation time τ_i (s)	Shear modulus g_i
1	0.000001	0.031920
2	0.000 01	0.055 066
3	0.000 1	0.094 570
4	0.001	0.148 209
5	0.01	0.203 485
6	0.1	0.212 089
7	1	0.146 179
8	10	0.068 084
9	100	0.025 889
10	1 000	0.008 865
11	10000	0.005084

The subgrade (embankment fill), extending sufficiently deep and laterally wide to minimize boundary influences, is modeled as an elastic solid medium with damping characteristics. To optimize computational resources, the FE model exploits symmetry about the track centerline, modeling only half of the track cross-section, and applies symmetry boundary conditions at the central vertical plane. Non-reflecting boundary conditions via ‘infinite elements’ are implemented along lateral and bottom boundaries, aiming to simulate an infinite subgrade domain.

Dynamic wheel–rail forces computed previously from the coupled vehicle–track dynamics model are sequentially introduced into the FE model at the rail nodes. This simulates the wheel loads traveling along the track in a moving manner. Forces are mapped onto nodal positions corresponding to instantaneous wheel locations, synchronized with the train speed and coupled dynamics outputs. A dynamic implicit analysis (direct time integration) with small time increments (e.g. $\Delta t = 1\times10^{-4}$ s) ensures accurate representation of load history and structural response.

The FE model predicts detailed substructure responses including vertical deflections of rails and sleepers, stress distributions within ballast and asphalt layers, and acceleration responses in the subgrade. By comparing cases with varying asphalt thicknesses or viscoelastic parameters, the influence of asphalt support layers on track dynamic behavior and overall structural integrity can be evaluated.

This sequential modeling approach (Figure 6), coupling the vehicle–track dynamics with a detailed FE substructure model, provides an effective and computationally efficient method for assessing the dynamic performance of railway ballasted track systems reinforced with asphaltic support layers.

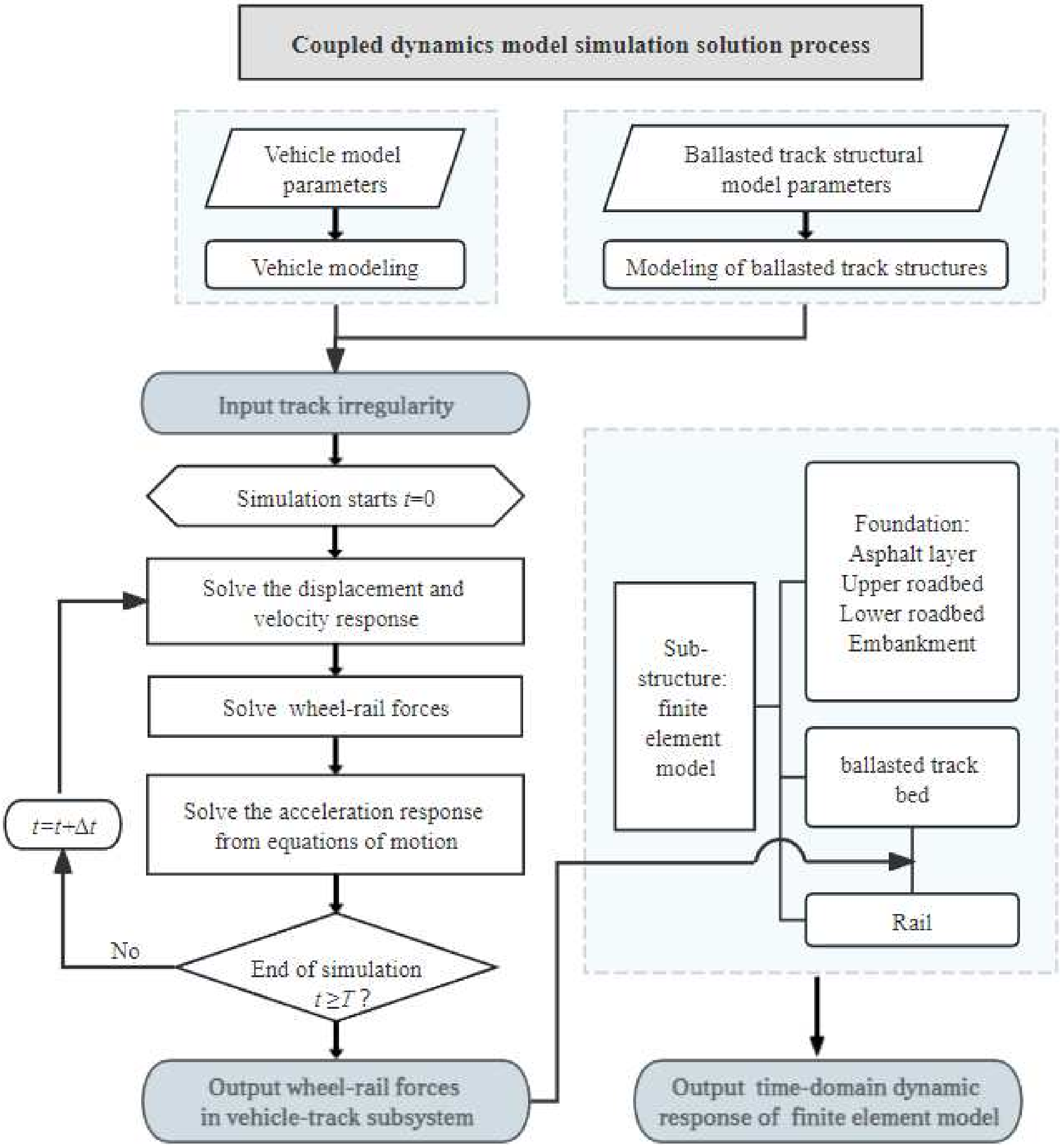

Figure 6. Flowchart of the integrated modeling framework.

3. Model Validation

The numerical model was validated using in-situ measurements from a trial section of the Beijing–Zhangjiakou high-speed railway – one of the first implementations of an ASL in a Chinese high-speed ballasted track.

3.1 Field site, instrumentation, and testing program

This double-track field site includes two adjacent track substructures: one ASL-improved trackbed and one conventional granular trackbed for direct comparison. In the ASL track, a 10 cm thick asphalt concrete layer was paved directly beneath the ballast, overlying 60 cm of compacted graded gravel fill (subgrade layer). The parallel standard track was built with a traditional 70 cm thick graded gravel subgrade and no asphalt layer. Above both substructures, the superstructure (i.e. ballast, sleepers, and rails) was identical. The ASL provides an additional stiff, impermeable layer intended to improve load distribution and waterproofing, thereby reducing subgrade deformation and long-term maintenance. The asphalt mixture used in the support layer is a dense-graded high-modulus hot-mix asphalt with low air-void content (≈3%), which enhances fatigue durability and water resistance. This mix offers high stiffness and load-spreading capability while retaining sufficient viscoelastic damping to attenuate vibrations. The field site's side-by-side configuration allows direct evaluation of ASL performance under high-speed train loading.

Figure 7 illustrates the instrumentation layout and trackbed cross-section of the test site. A total of 14 sensors were installed across the two sections (7 per track), including earth pressure cells for stress and integrated vibration transducers for movement. The sensors were embedded at the subgrade surface near the sleeper ends (directly beneath the rail seats) to capture the maximum vertical stress and vibration transmitted through the ballast. In the ASL section, each pressure cell was placed flush at the top of the graded gravel layer, just below the 10 cm asphalt layer, with a thin layer of standard sand packed around it to ensure proper coupling. All instruments were calibrated in the laboratory prior to installation to ensure accurate amplitude and frequency response. The earth pressure cells have a measurement range covering the expected stress pulses (on the order of hundreds of kPa) with high sensitivity, and the vibration sensors (triaxial geophones co-located with the pressure cells) measure ground motion velocity and acceleration up to ≈250 Hz. Data acquisition was performed at a high sampling rate to capture the rapid loading from passing axles.

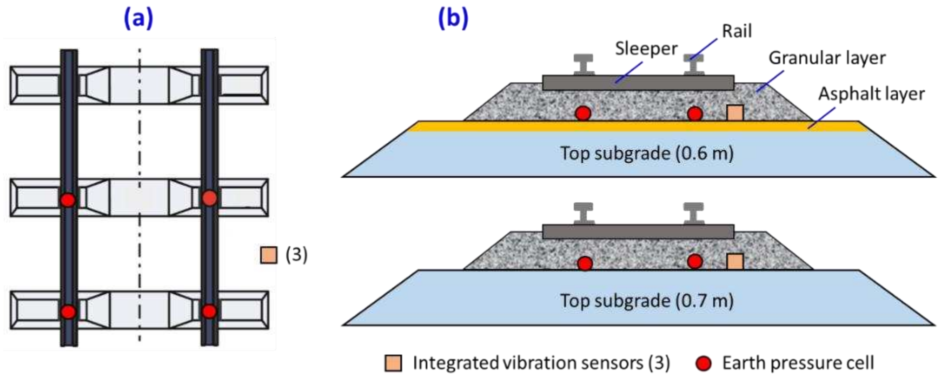

Figure 7. Instrumentation layout at the test site: (a) plan view; (b) cross-section.

Controlled test runs were conducted using a CRH380AJ high-speed inspection train during the railway’s commissioning phase (as shown in Figure 8). This eight-car electric multiple unit (CRH380A series) has 16 bogies (32 axles in total), providing a series of dynamic loading pulses as it travels. The train was run multiple times at increasing speeds from as low as 10 km/h up to 295 km/h. At each speed, the full train passage was recorded by the instrumentation, capturing the evolution of dynamic response with velocity. The highest test speed of 295 km/h is close to the maximum linespeed, enabling validation of the model under near–design speed loading. During each pass, the sensors measured the vertical stress time histories at the subgrade surface and the corresponding vibration (velocity and acceleration) induced in the foundation. The result was a comprehensive dataset of stress and vibration under known train loads, against which the numerical simulation results could be compared.

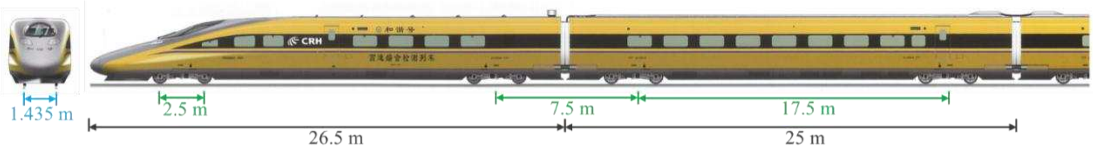

Figure 8. Configuration of the CRH380AJ-0203 inspection train used for validation tests.

3.2 Comparison of simulated and measured responses

1) Vertical Stress Response: The field-measured stress time history on the subgrade surface of the ASL-reinforced track shows a distinctive pattern of repeated “M-shaped” pulses as the train passes. Each two-axle bogie generates a characteristic double-peak in the stress signal, with two high stress peaks in quick succession (caused by the two-wheel axles of the bogie) followed by a brief valley. This pattern is clearly visible in the recorded waveform and aligns with the known bogie axle spacing. The numerical model successfully reproduces this behavior (Figure 9). The simulated vertical stress under the ASL track exhibits the same sequence of double-peaked bogie signatures, closely matching the field data in both timing and magnitude. Indeed, prior studies have noted that the number of stress peaks in a time history correspond directly to the train’s axle count, and the model captures this one-to-one correspondence. Quantitatively, the peak vertical stress beneath the sleeper ends in the asphalt-stabilized subgrade is of the order of tens of kPa per axle; the model-predicted peak values agree within a few percent of the measured maxima. The small trough between the two axle peaks (the center of the “M” shape) is also well-represented by the simulation, indicating the model accounts for the transient stress reduction as the bogie center passes. Figure 9 compares the measured and simulated stress waveforms, showing agreement in the shape of the pulses and the spacing between successive peaks (which is governed by the train’s bogie and car distances). Minor discrepancies in peak amplitude (on the order of ≈5–10% of the peak value) can be observed for some axles, which may be attributed to slight differences in load distribution or measurement noise. Overall however, the correspondence in the waveform characteristics – including peak magnitudes, valleys, and pulse durations – demonstrates that the model accurately reproduces the vertical stress response of the ASL track under high-speed loading.

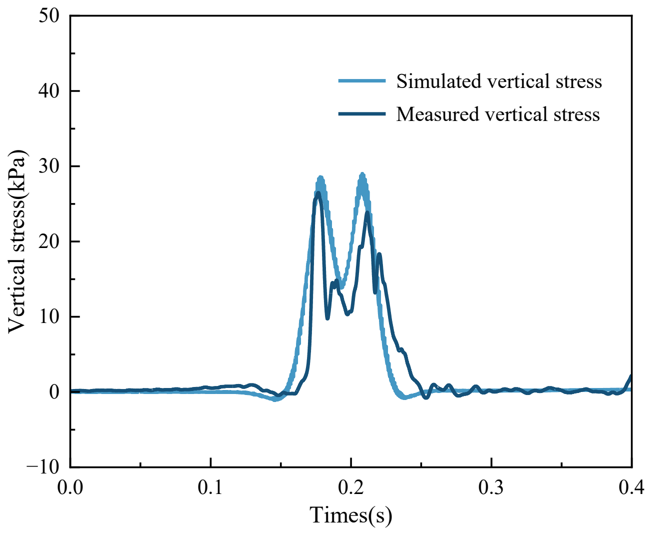

Figure 9. Comparison of simulated and measured vertical stress time histories beneath the ASL.

2) Vertical Vibration (Velocity) Response: The subgrade vibration induced by the train was analyzed in terms of vertical particle velocity. The field measurements in the ASL section show that as each axle load is applied, the subgrade experiences a sharp upward velocity impulse followed by oscillatory decay before the next axle arrives. The time-domain velocity profile thus consists of a series of oscillating spikes, reflecting the passage of each wheel. This is visible in the recorded velocity waveform (Figure 10), where the signal oscillates about zero with increasing amplitude when the train approaches, peaks as the fastest coaches pass over, and then decays. The numerical model's prediction of subgrade vibration aligns with the measured data. Figure 10 indicates that the simulation captures the amplitude of the velocity pulses and the inter-pulse oscillations. Both measured and simulated velocity records exhibit similar dominant frequencies of vibration in the subgrade, a result of the track–ground system's natural frequency and the periodic loading from the sleepers. Notably, the model correctly reproduces the slight increase in vibration amplitude observed in the asphalt-stiffened trackbed. In the field, the ASL section showed marginally higher peak particle velocities and accelerations than the adjacent conventional section, due to the greater track stiffness and lower damping of the asphalt layer. The simulation, which incorporates the asphalt layer's material properties (high stiffness and modest material damping), likewise predicts this increase. For example, the dynamic amplification factor for subgrade acceleration in the asphalt section was measured to be 1.66 (i.e. 66% higher than static loading) versus 1.56 in the granular section. The model produced a similar ratio, confirming that it captures the effect of the ASL on amplifying high-frequency responses. The close agreement between measured and computed velocity time histories – in terms of peak values (within ≈0.5 mm/s of each other), phase, and decay rate of oscillations – further corroborates the model's accuracy. Any phase shifts or extra high-frequency content in the measured signal (potentially due to wheel irregularities exciting the track) are also reflected to a reasonable extent in the simulation, owing to the model's inclusion of realistic track stiffness and damping parameters.

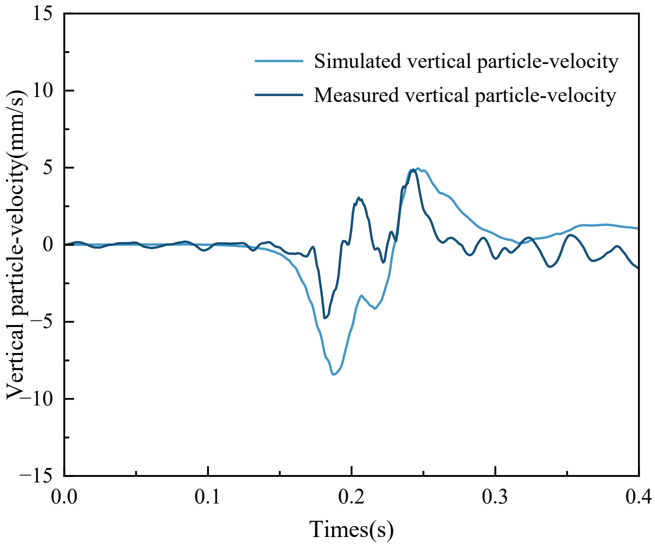

Figure 10. Comparison of simulated and measured vertical particle-velocity responses beneath the ASL.

4. Dynamic Response Analysis

Taking a fully loaded vehicle axle load of 14 t, train speed of 350 km/h, cumulative probability of track irregularity (λ = 0.632), and an ambient temperature of 15°C as standard conditions, this section investigates the dynamic response characteristics of an asphalt-reinforced ballasted trackbed.

4.1 Standard conditions

Figure 11 illustrates the transverse distribution of dynamic stress within the ASL and the graded gravel layer, extracted when the bogie center reaches the longitudinal midpoint of the FE model.

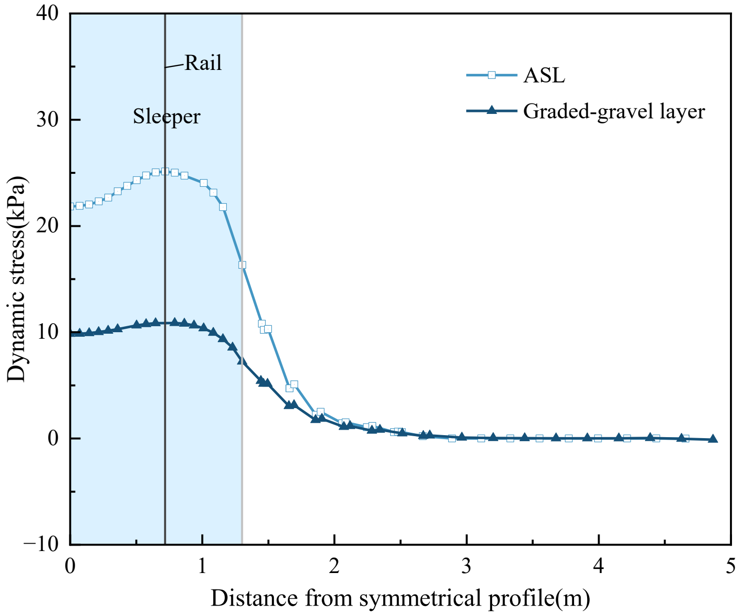

Figure 11. Transverse distribution of dynamic stress in the ASL and graded-gravel layer under standard loading conditions.

When the leading bogie is centered in the FE domain, both structural layers exhibit a broad plateau of compressive stress that extends from the track centre-line to approximately the rail-seat width (≈0.9 m). Within this region the ASL carries the highest load, peaking at −25.15 kPa directly beneath the rail. The overlying ballast spreads part of that load so that the graded-gravel layer experiences a reduced maximum of −10.88 kPa, corresponding to a 56.7% attenuation. Beyond the sleeper edge the stresses in both layers decline rapidly and vanish at ≈2.0 m, indicating effective lateral load redistribution by the sleeper – ballast – ASL assembly. The steeper gradient observed in the ASL curve between 1.0 m and 1.8 m reflects its higher stiffness: once the stress falls below roughly 5 kPa the asphalt layer off-loads almost entirely onto the surrounding ballast, whereas the more compliant graded gravel continues to carry small residual stresses until the ballast shoulder. This behaviour is similar to the widely reported “beam-on-elastic-layer” response in which a stiff interlayer concentrates load under the rail seat but also promotes faster lateral dissipation compared with a fully granular foundation.

Depth-wise, for the vertical stress decay with depth (Figure 12), stresses diminish in a strongly nonlinear manner. The most pronounced drop (≈53%) occurs across the ASL/graded-gravel interface, where the modulus falls from 1.6 GPa (asphalt) to 0.2 GPa (gravel). Below the graded gravel, stresses continue to dissipate but at a slower rate, confirming the asphalt layer absorbs the bulk of the dynamic excitation before it reaches the subgrade. At a depth of 3 m the vertical stress has fallen below 5 kPa, well inside typical service limits for HSR subgrades, and at a depth of 6 m it is negligible. These results emphasize the ASL's dual role as both a stress-spreading slab and a stiff "cap" that shields the underlying earthwork from high-frequency loads.

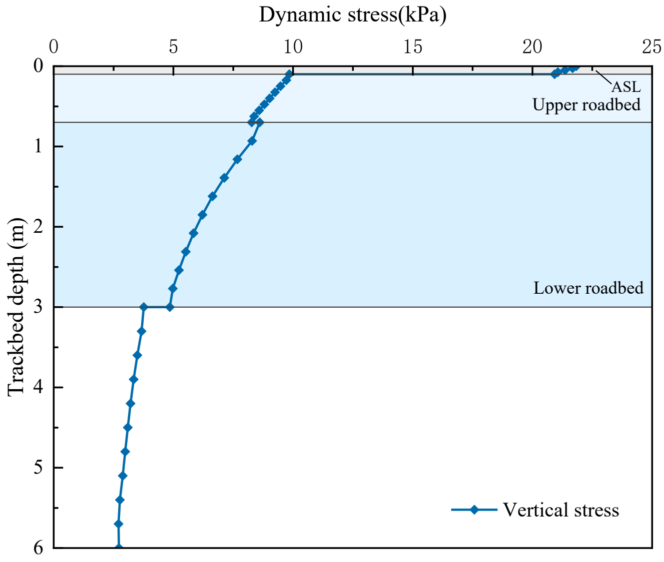

Figure 12. Vertical distribution of dynamic stress along the trackbed depth under standard loading conditions.

Figure 13 depicts the transverse distribution of dynamic displacement in the ASL and the graded gravel layer, again taken as the bogie center reaches the FE model's longitudinal midpoint. Despite the strong contrast in stress levels, the displacement curves for the two layers are almost coincident. The maximum dynamic deflection under the rail seat is −0.19 mm, tapering smoothly to zero at ≈4.5 m from the centre-line. The near-perfect overlap implies that the overall vertical compliance of the trackbed is dominated by the ballast and subgrade system; the ASL's added stiffness changes local stresses without markedly altering global deflection. From a maintenance standpoint, this is advantageous: settlement behaviour remains governed by ballast–subgrade interaction, while the asphalt layer acts primarily as a stress buffer. The modest peak value (< 0.2 mm) also satisfies commonly used serviceability criteria for high-speed lines (< 0.5 mm dynamic rail deflection), indicating adequate track stiffness.

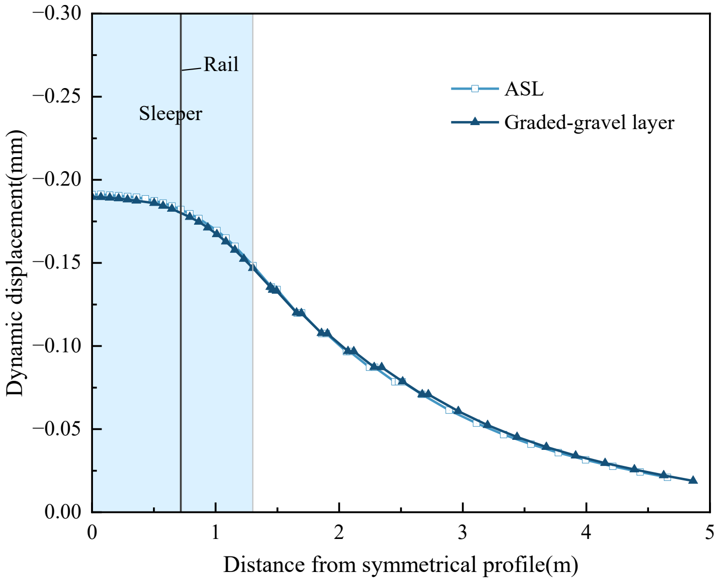

Figure 13. Transverse distribution of dynamic displacement in the ASL and graded-gravel layer under standard loading conditions.

The transverse distribution of vertical acceleration for both ASL and graded gravel layers under the standard condition is presented in Figure 14. Peak negative accelerations occur at the rail seat (−0.15 m s^{-2} in the ASL and −0.12 m s^{-2} in the graded gravel) before decaying almost linearly toward the ballast shoulder. The slightly higher magnitude in the asphalt layer reflects its reduced damping and higher natural frequency compared with the granular fill. Nevertheless, the difference is minor (≈ 0.03 m s^{-2}), suggesting the asphalt's viscoelastic damping (modeled via the Prony series) is sufficient to prevent excessive vibration amplification. The gradual decay implies effective energy dissipation within the ballast. No local resonances or standing waves are observed, which would otherwise manifest as secondary peaks in the acceleration trace.

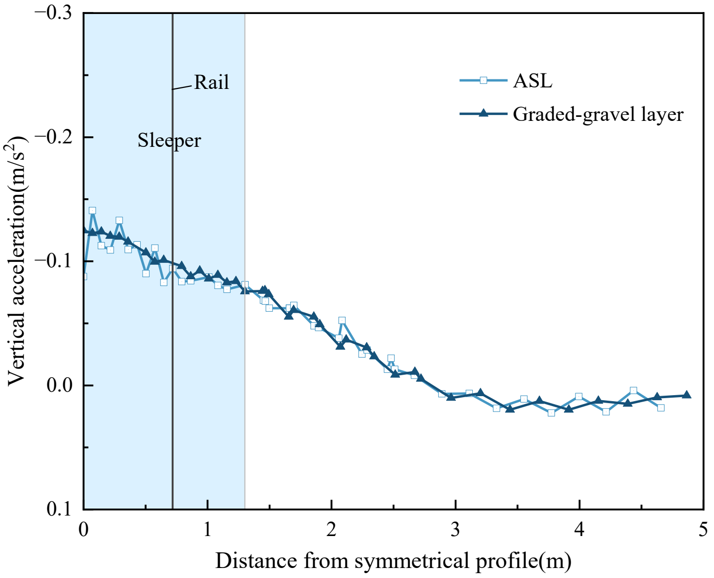

Figure 14. Transverse distribution of vertical acceleration in the ASL and graded-gravel layer under standard loading conditions.

Together, Figures 11–14 demonstrate that a 10 cm ASL lowers subgrade stresses while preserving global stiffness and keeping vibration levels within acceptable limits. The sharp stress reduction at the asphalt–gravel interface confirms that the chosen thickness is already sufficient to exploit most of the stress-attenuation potential; thicker layers would yield diminishing returns in stress reduction yet add cost and construction complexity. Conversely, the negligible impact on displacement and modest increase in acceleration indicate that the asphalt layer does not introduce serviceability penalties such as excessive settlement. These findings substantiate the earlier recommendation that a 10 cm dense-graded high-modulus asphalt layer offers the optimal balance between structural performance and quantity of material for high-speed ballasted tracks.

4.2 Influence of track-irregularity severity

To isolate the role of track geometry in governing foundation response, two probabilistic irregularity levels were imposed on the vehicle–track model: λ = 0.632, representative of an average high-speed line, and λ = 0.99, representing a near-worst-case profile. Each was evaluated at the design speed (350 km/h) and at a slow speed (5 km/h) so that dynamic magnification effects could be separated from pure geometric uplift. Peak dynamic stresses at the rail projection position are summarized in Table 3.

Table 3. Peak dynamic stresses under varying track-irregularity conditions.

Train speed	Irregularity level	Peak stress in ASL (kPa)	Peak stress in graded gravel (kPa)	Stress-attenuation efficiency*
350 km/h	λ=0.632	−26.16	−23.91	8.6%
350 km/h	λ=0.99	−26.49	−24.97	5.7%
5 km/h	λ=0.632	−26.20	−23.63	9.8%
5 km/h	λ=0.99	−26.20	−23.70	9.5%

Note: *Efficiency = (ASL peak − gravel peak) / |ASL peak| × 100 %.

Some key observations from Table 3: At 350 km/h, raising λ from 0.632 to 0.99 increases the gravel-layer peak stress by 4.4% (from −23.91 kPa to −24.97 kPa), whereas the ASL peak rises by only 1.3 %. Also, at 5 km/h, the same increase in λ elevates gravel stress by only 0.3 %. Stress-reduction efficiency drops from 8.6 % to 5.7% when λ escalates to 350 km/h, a relative decline of ≈33 % (Figure 15). In contrast, efficiency remains nearly constant at low speed, underscoring that the ASL's protective capacity is more vulnerable to irregularity-driven dynamic effects than to the geometric irregularities themselves. Even under the most adverse combination tested ($\lambda = 0.99$, 350 km/h), the ASL trims roughly 1.5 kPa from the peak stress that would otherwise reach the sub-ballast. While modest in percentage terms, this reduction is meaningful because ballast fatigue and fouling rates are highly stress-sensitive; field studies report that each kilopascal cut in cyclic stress can translate into several millimeters less annual settlement. The viscoelastic ASL acts as a stiff, lightly damped plate. At low speeds its high bending stiffness spreads the quasi-static rail load effectively, largely independent of irregularity amplitude. At high speeds however, irregularities excite wheel–rail resonance, injecting higher-frequency content (> 15 Hz) that is less efficiently dispersed by the slab and is instead transmitted more directly to the ballast interface, eroding attenuation efficiency.

Because the ASL's benefit is most compromised by roughness-induced dynamics at high speed, stringent geometric-quality control (grinding and tamping) remains essential for lines adopting asphalt reinforcement. A drop of attenuation efficiency from ≈9% toward ≈5% can be used as an early-warning indicator for irregularity growth, prompting corrective maintenance before gravel stresses breach service limits. The data suggest that increasing slab thickness would yield only diminishing marginal gains under severe irregularity; therefore, resources are better spent on proactive track-geometry management than on oversizing the ASL.

Figure 15 summarizes these findings visually: higher λ values shorten the "stress-reduction bar," especially at 350 km/h, whereas the dark-blue bars (high λ) at 5 km/h remain mostly unchanged. This divergence reinforces the conclusion that speed–irregularity coupling, rather than roughness alone, governs the stress-shielding performance of a 10 cm ASL.

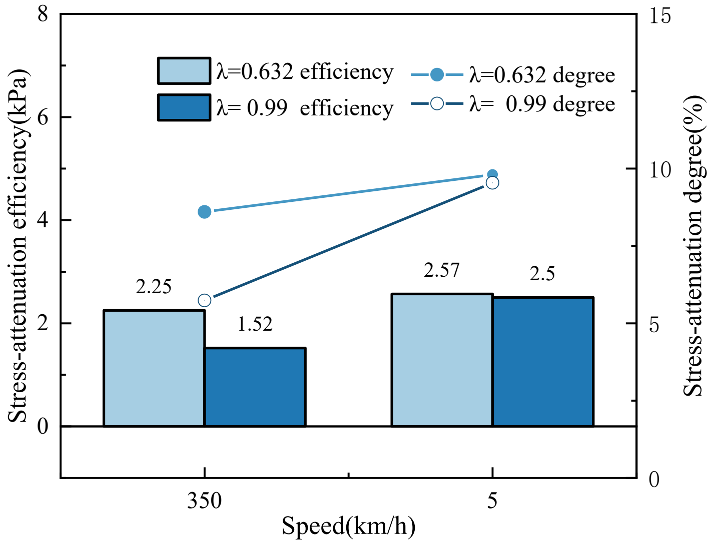

Figure 15. Effect of track-irregularity severity on stress-attenuation efficiency of a 10 cm ASL at 5 km/h and 350 km/h

4.3 Influence of asphalt-layer parameters

Parametric studies were conducted to analyze the effects of asphalt layer thickness and environmental temperature on the dynamic response of the reinforced track structure. Peak dynamic stresses for various ASL thicknesses (8, 10, 12, 15 cm) at standard conditions (350 km/h, λ=0.632, 15 °C) are shown in Table 4.

Table 4. Peak dynamic stresses for varying ASL thicknesses at 350 km/h and λ = 0.632

Thickness (cm)	Δσ* (kPa)	Attenuation efficiency†
8	1.67	6.4%
10	2.59	9.9%
12	3.08	11.8%
15	3.42	13.2%

Note: $*\Delta\sigma = |\sigma_{ASL}| - |\sigma_{gravel}|$; † $\Delta\sigma / |\sigma_{ASL}|$.

Increasing the ASL thickness from 8 cm to 15 cm produces a nearly linear rise in stress-reduction amplitude (Figure 16), but the incremental benefit diminishes beyond 12 cm. A thicker slab increases bending stiffness ($\propto h^3$) and contact area, spreading wheel loads more effectively so that less stress penetrates into the ballast. The slope of Δσ flattens after 12 cm (gain of 0.34 kPa from 12 → 15 cm vs. 0.92 kPa from 8 → 10 cm). This is because once the slab stiffness far exceeds that of the ballast, further increases predominantly stiffen the rail–slab system rather than improving load distribution. The 10 cm layer captures approximately 75 % of the maximum feasible attenuation (2.59 kPa vs. 3.42 kPa at 15 cm) while avoiding the added material cost and dual-lift paving required for thicker sections.

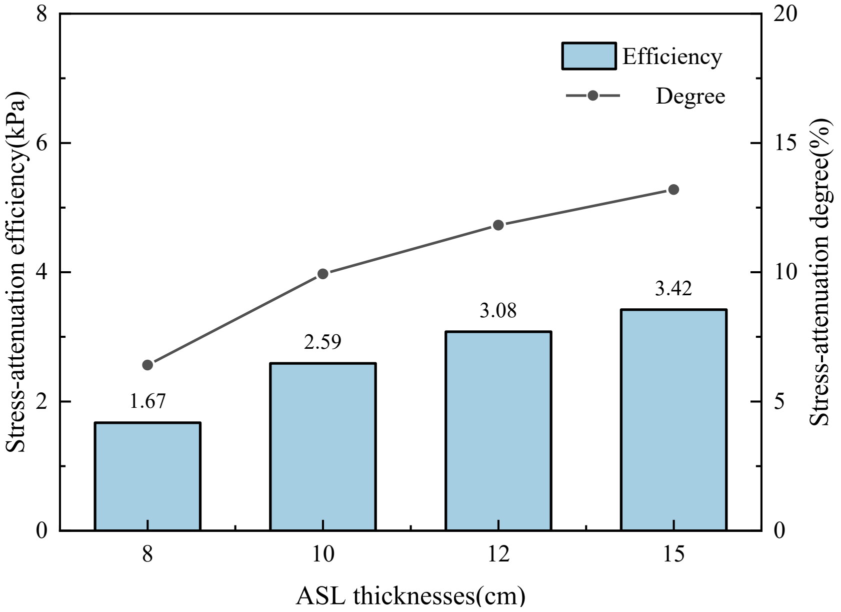

Figure 16. Influence of ASL thickness on stress-attenuation efficiency at 350 km/h and λ = 0.632

The impact of environmental temperatures (5, 15, 25, 35 °C) on peak dynamic stresses is summarized in Table 5. Ambient temperature alters asphalt stiffness through time–temperature superposition; as temperature rises, the complex modulus drops and the slab behaves more like a viscoelastic mat than a rigid plate.

Table 5. Peak dynamic stresses under varying temperatures

Temperature (°C)	σ_{ASL} (kPa)	σ_{gravel} (kPa)	Δσ (kPa)	Efficiency
5	−27.28	−24.36	2.92	10.7%
15 (reference)	−26.17	−23.51	2.66	10.2%
25	−23.83	−21.76	2.07	8.7%
35	−19.49	−18.03	1.46	7.5%

As illustrated in Figure 17, both asphalt and gravel stresses decline with temperature because the softer slab allows greater system deflection, which lengthens load-application time and reduces peak forces. Nevertheless, attenuation efficiency drops by ≈30% (10.7 → 7.5 %) as the modulus contrast between slab and ballast narrows. At 35 °C the slab's natural frequency approaches that of the ballast–rail system, reducing its filtering capability and allowing more of the high-frequency load content to reach the gravel layer. The lowest efficiency of 7.5 % still reduces 1.46 kPa from the ballast peak, sufficient to keep stresses below the 30–35 kPa fatigue threshold commonly cited for high-speed ballast. However, where sustained pavement temperatures exceed 35 °C (e.g. subtropical climates), the results suggest combining the 10 cm slab with polymer-modified binders or surface cooling strategies to preserve stiffness.

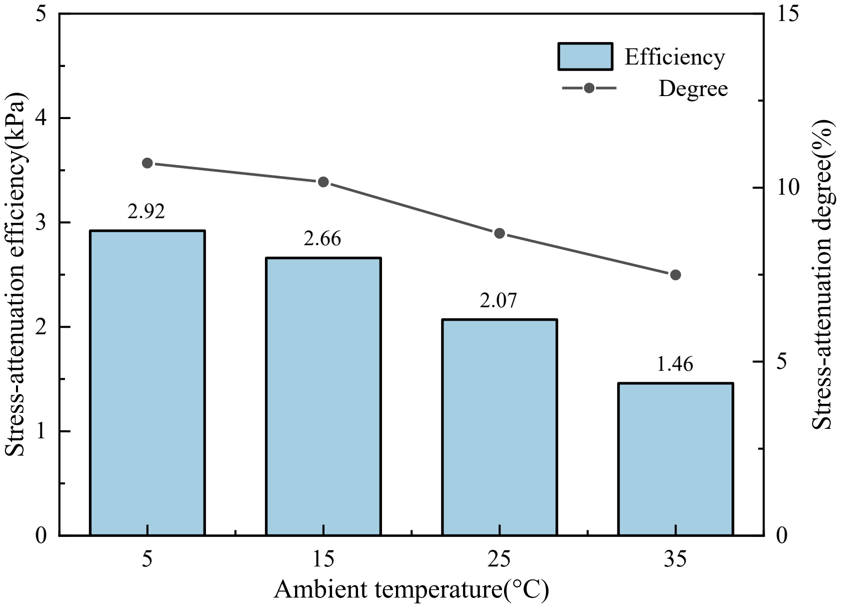

Figure 17. Influence of ambient temperature on stress-attenuation efficiency of a 10 cm ASL.

The modest loss of efficiency at elevated temperatures can be partially offset by an additional 2 cm of thickness: moving from 10 → 12 cm at 35 °C would raise $\Delta\sigma$ from 1.46 → ≈2.0 kPa (by linear interpolation of Figure 16), restoring performance to the 25 °C baseline. For temperate regions (5–25 °C design air temperature) a single-lift 10 cm dense-graded high-modulus asphalt layer provides a near-optimal balance of stress mitigation, constructability, and life-cycle cost. In hot regions, designers may consider either increasing the thickness to 12 cm or specifying a stiffer binder grade to maintain ≥ 9 % attenuation efficiency without excessive thickness.

These findings reinforce that ASL performance is governed by the stiffness contrast with the ballast rather than by absolute stiffness alone. Consequently, rational ASL design should explicitly account for seasonal modulus variation and diminishing benefit beyond approximately 12 cm thickness.

5. Durability and Stability Evaluation

Fatigue cracking and permanent deformation are the primary control indices in asphalt pavement design. According to [20], the horizontal tensile strain (ε_r) at the bottom of the ASL governs fatigue cracking, while the vertical compressive strain (ε_z) at the surface controls resistance to permanent deformation. In this study, although the loading scenario differs from highway pavements, where asphalt directly bears vehicle loads, train loads transmitted through the rail structure induce similar stresses and strains in the ASL due to comparable material properties. Thus, tensile strain at the bottom and compressive strain at the top of the ASL are employed to assess the layer's durability against fatigue damage and permanent deformation.

5.1 Durability analysis of asphaltic support layers

Given that the viscoelastic behavior of asphalt concrete depends on ambient temperature, fatigue and permanent deformation, damage must be separately evaluated for each season. The annual fatigue and permanent deformation damage are then computed by summing seasonal values according to Equations (9) and (10):

$$m_a = \sum_{i=1}^{4} m_{ai} = \sum_{i=1}^{4} \frac{N_i}{N_{ai}} \tag{9}$$

$$m_s = \sum_{i=1}^{4} m_{si} = \sum_{i=1}^{4} \frac{N_i}{N_{si}} \tag{10}$$

where m_{ai} and m_{si} are seasonal fatigue and permanent deformation damage, respectively; N_i represents the number of bogie load cycles per season; and N_{ai} and N_{si} are the allowable number of load cycles corresponding to seasonal fatigue and permanent deformation damage, respectively.

Here, seasonal ambient temperatures are represented by 15 °C for spring, 35 °C for summer, 25 °C for autumn, and 5 °C for winter. Taking ASL thicknesses of 8, 10, 12, and 15 cm at an ambient temperature of 15 °C as an example, the horizontal and longitudinal strain time histories at the bottom of the ASL, after smoothing, are presented in Figure 18.

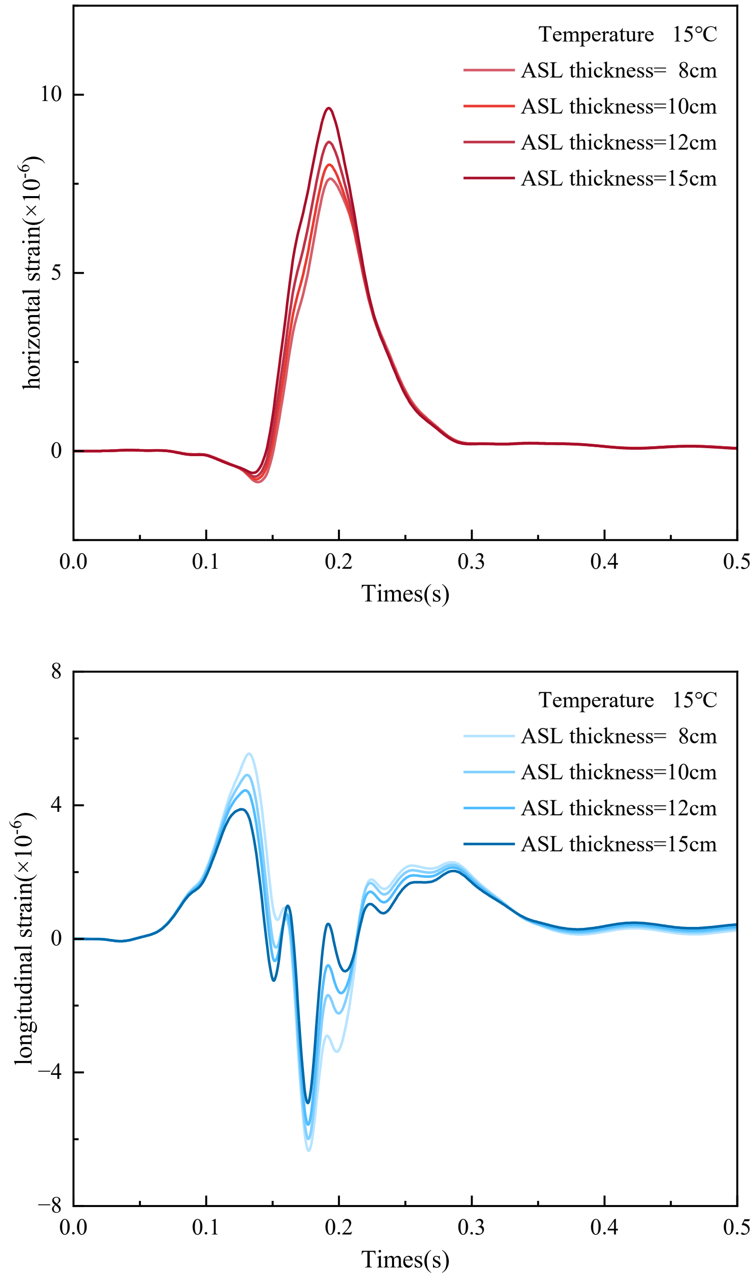

Figure 18. Dynamic strain time histories at the bottom of the ASL: (a) horizontal strain; (b) longitudinal strain.

Similar to previous findings for slab tracks, the dominant strain is horizontal tensile strain. Thus, the horizontal strain represents the maximum tensile strain (ε_r). The maximum vertical compressive strain at the top of the ASL (ε_z) is selected to evaluate permanent deformation. The results of durability assessments for reinforcement thicknesses of 8, 10, 12, and 15 cm are summarized in Tables B1-B4 (Appendix).

As shown in Tables B1-B4, the fatigue and permanent deformation damages decrease with increasing thickness of the asphalt reinforcement layer from 8 cm to 15 cm. Furthermore, all listed thicknesses yield cumulative fatigue and permanent deformation damages below 1.0 for a 100-year design service life, indicating that the durability of the ASL meets the serviceability requirements within the evaluated thickness range.

5.2 Stability assessment of trackbed

According to [21], cumulative plastic deformation in high-speed railway trackbeds should be prevented, and the vertical elastic strain in the upper and lower layers of the trackbed must not exceed threshold values corresponding to rapid strain convergence conditions. Based on empirical relationships from [22], which link the elastic strain threshold of coarse granular fills to the modulus of subgrade reaction (K_{30}), the elastic modulus and corresponding stress thresholds for different values of K_{30} are calculated and listed in Table 6.

Table 6. Stress thresholds of coarse fills for different moduli of subgrade reaction (K_{30}).

K_{30} (MPa/m)	Elastic modulus (MPa)	Strain threshold (με)	Stress threshold (kPa)
190	228.72	160.2	36.64
180	218.23	157.4	34.35
170	207.59	154.6	32.09
160	196.80	151.8	29.87
150	185.85	149.0	27.69
140	174.73	146.2	25.55
130	163.46	143.4	23.44
120	152.01	140.6	21.37
110	140.39	137.8	19.35
100	128.60	135.0	17.36
90	116.62	132.2	15.42

Linear interpolation based on the data in Table 6 is conducted to determine the threshold moduli of subgrade reaction ([K_{30}]) from the calculated dynamic stresses at the surface of the graded gravel layer and bottom of the trackbed. Figure 19 presents the variations of dynamic stresses and the corresponding threshold moduli of subgrade reaction with different thicknesses of the ASL.

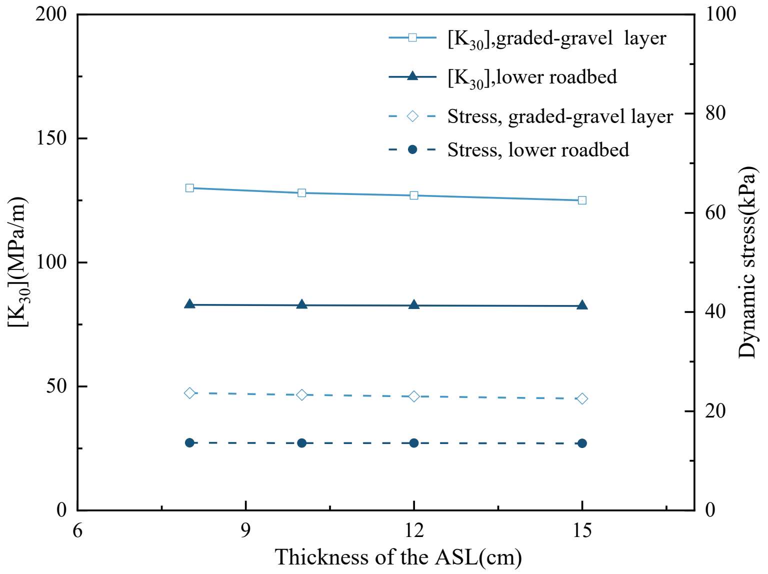

Figure 19. Influence of ASL thickness on dynamic stress and the corresponding threshold K_{30}.

ASL thickness notably influences dynamic stresses and corresponding threshold moduli. Increasing the thickness of the ASL reduces dynamic stresses at the surfaces of both the graded gravel and lower subgrade layers, a trend consistent with observations in slab track structures. According to the current specifications, the required minimum K_{30} values are 190 MPa/m for the upper trackbed layer and between 130 and 150 MPa/m for the lower trackbed layer. For all evaluated thicknesses (8, 10, 12, 15 cm), the minimum calculated moduli of subgrade reaction, 132 MPa/m for the graded gravel layer and 83.10 MPa/m for the lower subgrade, are lower than the prescribed values. This indicates that adopting an ASL as a waterproofing and sealing structure significantly relaxes the design standards required for underlying trackbed materials.

Although thicker ASLs improve structural performance, they also raise material costs. Additionally, thicknesses beyond 10 cm typically require dual-layer construction, increasing complexity. Consequently, a 10-cm thick ASL is recommended as the optimal solution, balancing performance and cost considerations.

6. Conclusions

This paper presented a numerical investigation into the dynamic response, durability, and stability of ballasted railway tracks reinforced with asphalt support layers (ASL), using an advanced coupled vehicle-track dynamics and 3D finite element modeling approach. Key findings are as follows:

1. A 10 cm ASL reduces subgrade peak dynamic stresses by $\approx$ 55% compared with a conventional graded-gravel layer, while vertical track displacements remain essentially unchanged (< 0.2 mm).
2. The ASL's stress-reduction efficiency declines as track irregularity amplitude (λ) rises from 0.632 to 0.99 and as ambient temperature increases from 5 °C to 35 °C. Nevertheless, the ASL consistently lowers peak stresses relative to a conventional section.
3. Raising ASL thickness from 8 cm to 15 cm improves stress attenuation, but the marginal gains beyond 10 cm do not justify potential added construction

complexity.

4. Cumulative fatigue cracking (ε_r-controlled) and permanent deformation (ε_z-controlled) indices remain well below unity for all tested thicknesses over a 100-year design horizon, confirming adequate long-term serviceability.
5. Computed K_{30} exceed specification limits for both upper and lower trackbed layers, indicating ASL reinforcement markedly relaxes material-quality requirements for the underlying fill.
6. A 10 cm dense-graded high-modulus ASL is recommended for HSR ballast tracks to achieve stress attenuation, robust durability, and satisfactory stability.

Acknowledgments

This study was supported by the Major Program of Natural Science Foundation of Sichuan Province of China (Grant No. 2024NSFSC0003), the Overseas Expertise Introduction Project for Discipline Innovation ("111 Project ", Grant No. B21011) and the UK’s Royal Society (IEC\NSFC\211306).

References

[1] Su,Q, Huang, JJ, Li, SY, Zhang, WC, Bai, H, Real-Time Monitoring and Early Warning Systems for Subgrade Settlement of High Speed Railway in Service Period, in: Hong Kong, PEOPLES R CHINA, 2011: pp. 139–142.

[2] M. Koohmishi, M. Palassi, Degradation of railway ballast under compressive loads considering particles rearrangement, Int. J. Pavement Eng. 21 (2020) 157–169. https://doi.org/10.1080/10298436.2018.1449949.

[3] S. Lobo-Guerrero, L.E. Vallejo, Discrete Element Method Analysis of Railtrack Ballast Degradation during Cyclic Loading, Granular Matter 8 (2006) 195–204. https://doi.org/10.1007/s10035-006-0006-2.

[4] Q. Luo, H. Fu, K. Liu, T. Wang, G. Feng, Monitoring of train-induced responses at asphalt support layer of a high-speed ballasted track, Constr. Build. Mater. 298 (2021) 123909. https://doi.org/10.1016/j.conbuildmat.2021.123909.

[5] X. Xiao, D. Cai, L. Lou, Y. Shi, F. Xiao, Application of asphalt based materials in railway systems: A review, Constr. Build. Mater. 304 (2021) 124630. https://doi.org/10.1016/j.conbuildmat.2021.124630.

[6] M. Fang, T. Hu, J.G. Rose, Geometric composition, structural behavior and material design for asphalt trackbed: A review, Constr. Build. Mater. 262 (2020) 120755. https://doi.org/10.1016/j.conbuildmat.2020.120755.

[7] Y. Momoya, E. Sekine, PERFORMANCE-BASED DESIGN METHOD FOR

RAILWAY ASPHALT ROADBED, Doboku Gakkai Ronbunshuu E 63 (2007) 608–619. https://doi.org/10.2208/jsceje.63.608.

[8] J.G. Rose, P.F. Teixeira, N.E. Ridgway, Utilization of Asphalt/Bituminous Layers and Coatings in Railway Trackbeds: A Compendium of International Applications, in: 2010 Joint Rail Conference, Volume 1, ASMEDC, Urbana, Illinois, USA, 2010: pp. 239–255. https://doi.org/10.1115/JRC2010-36146.

[9] D. Ramirez Cardona, H.D. Benedetto, C. Sauzeat, N. Calon, J.G. Rose, Designs, Application and Performances of Asphalt/Bituminous Trackbeds in European, Asian, and African Countries, Transp. Res. Rec.: J. Transp. Res. Board 2674 (2020) 245–262. https://doi.org/10.1177/0361198120945314.

[10] G. Martinez-Arguelles, F. Giustozzi, M. Crispino, G.W. Flintsch, Investigating physical and rheological properties of foamed bitumen, Constr. Build. Mater. 72 (2014) 423–433. https://doi.org/10.1016/j.conbuildmat.2014.09.024.

[11] F. Gschösser, H. Wallbaum, Life Cycle Assessment of Representative Swiss Road Pavements for National Roads with an Accompanying Life Cycle Cost Analysis, Environ. Sci. Technol. (2013) 130718092515005. https://doi.org/10.1021/es400309e.

[12] D. Ramirez Cardona, H. Di Benedetto, C. Sauzeat, N. Calon, G. Saussine, Use of a bituminous mixture layer in high-speed line trackbeds, Constr. Build. Mater. 125 (2016) 398–407. https://doi.org/10.1016/j.conbuildmat.2016.07.118.

[13] G. Di Mino, M. Di Liberto, C. Maggiore, S. Noto, A Dynamic Model of Ballasted Rail Track with Bituminous Sub-Ballast Layer, Procedia - Soc. Behav. Sci. 53 (2012) 366–378. https://doi.org/10.1016/j.sbspro.2012.09.888.

[14] Q. Ye, Q. Luo, D.P. Connolly, T. Wang, H. Xie, H. Ding, The effect of asphaltic support layers on slab track dynamics, Soil Dyn. Earthquake Eng. 166 (2023) 107771. https://doi.org/10.1016/j.soildyn.2023.107771.

[15] Q. Ye, G. Feng, Q. Luo, T. Wang, Shakedown Limit Analysis of Asphaltic Support Layers for Railway Slab Tracks, in: C. Rujikiatkamjorn, J. Xue, B. Indraratna (Eds.), Proceedings of the 5th International Conference on Transportation Geotechnics (ICTG) 2024, Volume 7, Springer Nature Singapore, Singapore, 2025: pp. 219–228. https://doi.org/10.1007/978-981-97-8237-6_22.

[16] Zhai Wanming, Vechicle-Track Coupled Dynamics, Fourth Edition, 北京：科学出版社, 2015.

[17] Lei Xiaoyan, High Speed Railway Track Dynamics:Models, Algorithm and Application, Second Edition, 北京：科学出版社, 2021.

[18] S. Liu, X. Chen, Y. Ma, J. Yang, D. Cai, G. Yang, Modelling and in-situ measurement of dynamic behavior of asphalt supporting layer in slab track system, Constr. Build. Mater. 228 (2019) 116776. https://doi.org/10.1016/j.conbuildmat.2019.116776.

[19] WILLIAMS M L, LANDEL R F, FERRY J D, The Temperature Dependence of Relaxation Mechanisms in Amorphous Polymers and Other Glass-forming Liquids, Journal of the American Chemical Society 77 (1955) 3701–3707.

[20] J.G. Rose, S. Liu, R.R. Souleyrette, KENTRACK 4.0: A Railway Trackbed Structural Design Program, in: 2014 Joint Rail Conference, American Society of Mechanical Engineers, Colorado Springs, Colorado, USA, 2014: p. V001T01A010. https://doi.org/10.1115/JRC2014-3752.

[21] T. Wang, Q. Luo, J. Liu, G. Liu, H. Xie, Method for slab track substructure design at a speed of 400 km/h, Transp. Geotech. 24 (2020) 100391. https://doi.org/10.1016/j.trgeo.2020.100391.

[22] Luo Q, Zhang R, Xie H, Tian D, Structural analysis and key parameter of

ballastless track subgrade for 400km·h-1 high-speed railway., China Railw Sci (2020) 34–44.

Appendix A

This part consolidates the key mechanical and geometric inputs employed in the coupled vehicle–track dynamics model. Table A1 lists the principal mass, inertia, and suspension properties of the eight-car CRH-380A inspection train that generates the dynamic wheel loads used throughout the study. Table A2 presents the corresponding rail, sleeper, ballast, and subgrade parameters—covering stiffness, damping, and mass per unit length—that define the vertical track subsystem. Together, these datasets ensure full reproducibility of the numerical simulations reported in Sections 2–4.

Table A1. Model Parameters of the CRH-380A Vehicle

Parameter	Symbol	Unit	Value
Vehicle body mass	M_c	kg	4.293×10^4
Vehicle body pitching inertia	J_c	$kg\cdot m^2$	1.712×10^6
Bogie frame mass	M_t	kg	3 300
Bogie pitching inertia	J_t	$kg\cdot m^2$	1 807
Wheelset mass	M_w	kg	1 780
Primary suspension stiffness	K_{pz}	$N\cdot m^{-1}$	1.2×10^6
Primary suspension damping	C_{pz}	$N\cdot s\cdot m^{-1}$	1.0×10^4
Secondary suspension stiffness	K_{sz}	$N\cdot m^{-1}$	2.4×10^5
Secondary suspension damping	C_{sz}	$N\cdot s\cdot m^{-1}$	2.0×10^4
Half-length between bogie centers	l_c	m	8.75
Half-length of fixed bogie axle spacing	l_t	m	1.25

Table A2. Parameters of Ballasted Track Model

Parameter	Symbol	Unit	Value
Rail elastic modulus	E	$N\cdot m^{-2}$	2.10×10^{11}
Rail moment of inertia	I_Y	m^4	4.49×10^{-5}
Rail mass per unit length	m_r	$kg\cdot m^{-1}$	74.41
Sleeper mass	M_s	kg	320
Rail pad vertical stiffness	K_p	$N\cdot m^{-1}$	6.00×10^7
Rail pad vertical damping	C_p	$N\cdot s\cdot m^{-1}$	7.50×10^4
Ballast mass	M_b	kg	360
Ballast vertical stiffness	K_b	$N\cdot m^{-1}$	2.25×10^8
Ballast vertical damping	C_b	$N\cdot s\cdot m^{-1}$	6.00×10^4
Ballast lateral shear stiffness	K_w	$N\cdot m^{-1}$	7.84×10^7
Ballast lateral shear damping	C_w	$N\cdot s\cdot m^{-1}$	8.00×10^4
Subgrade discrete stiffness	K_f	$N\cdot m^{-1}$	2.43×10^8
Subgrade discrete damping	C_f	$N\cdot s\cdot m^{-1}$	1.00×10^5

Appendix B

Durability assessments were conducted using seasonal ambient temperatures of 15 °C (spring), 35 °C (summer), 25 °C (autumn), and 5 °C (winter). Tensile strain at the bottom of the ASL, ε_r, was taken as the maximum horizontal tensile strain, while compressive strain at the top of ASL, ε_z, was taken as the maximum vertical compressive strain. The results of durability evaluations for ASL thicknesses of 8, 10, 12, and 15 cm are summarized in Tables B1, B2, B3, and B4, respectively.

Table B1. Fatigue and permanent-deformation assessment for an 8 cm ASL.

Index	5 °C	15 °C	25 °C	35 °C
ε_r	8.81×10^{-6}	8.89×10^{-6}	8.87×10^{-6}	8.54×10^{-6}
N_{ai}	1.03×10^{12}	1.01×10^{12}	1.01×10^{12}	1.15×10^{12}
m_{ai}	2.64×10^{-7}	2.71×10^{-7}	2.69×10^{-7}	2.38×10^{-7}
ε_z	1.35×10^{-5}	1.77×10^{-5}	3.00×10^{-5}	5.55×10^{-5}
N_{si}	8.73×10^{12}	2.58×10^{12}	2.41×10^{11}	1.54×10^{10}
m_{si}	3.13×10^{-8}	1.06×10^{-7}	1.13×10^{-6}	1.77×10^{-5}
m_a		0.00000104		
m_s		0.00001900		

Table B2. Fatigue and permanent-deformation assessment for a 10 cm ASL.

Index	5 °C	15 °C	25 °C	35 °C
ε_r	8.56×10^{-6}	8.68×10^{-6}	8.72×10^{-6}	8.44×10^{-6}
N_{ai}	1.14×10^{12}	1.09×10^{12}	1.07×10^{12}	1.19×10^{12}
m_{ai}	2.39×10^{-7}	2.51×10^{-7}	2.55×10^{-7}	2.29×10^{-7}
ε_z	1.33×10^{-5}	1.75×10^{-5}	2.99×10^{-5}	5.55×10^{-5}
N_{si}	9.16×10^{12}	2.71×10^{12}	2.46×10^{11}	1.54×10^{10}
m_{si}	2.98×10^{-8}	1.01×10^{-7}	1.11×10^{-6}	1.78×10^{-5}
m_a		0.00000097		
m_s		0.00001902		

Table B3. Fatigue and permanent-deformation assessment for a 12 cm ASL.

Index	5 °C	15 °C	25 °C	35 °C
ε_r	8.18×10^{-6}	8.30×10^{-6}	8.40×10^{-6}	8.21×10^{-6}
N_{ai}	1.32×10^{12}	1.26×10^{12}	1.21×10^{12}	1.31×10^{12}
m_{ai}	2.06×10^{-7}	2.17×10^{-7}	2.25×10^{-7}	2.09×10^{-7}
ε_z	1.32×10^{-5}	1.74×10^{-5}	2.98×10^{-5}	5.55×10^{-5}
N_{si}	9.49×10^{12}	2.80×10^{12}	2.50×10^{11}	1.54×10^{10}
m_{si}	2.88×10^{-8}	9.75×10^{-8}	1.09×10^{-6}	1.77×10^{-5}
m_a		0.00000086		
m_s		0.00001889		

Table B4. Fatigue and permanent-deformation assessment for a 15 cm ASL.

Index	5 °C	15 °C	25 °C	35 °C
ε_r	7.91×10^{-6}	8.02×10^{-6}	8.01×10^{-6}	7.97×10^{-6}
N_ai	1.47×10^{12}	1.41×10^{12}	1.42×10^{12}	1.44×10^{12}
m_ai	1.85×10^{-7}	1.93×10^{-7}	1.92×10^{-7}	1.89×10^{-7}
ε_z	1.31×10^{-5}	1.72×10^{-5}	2.96×10^{-5}	5.54×10^{-5}
N_si	9.91×10^{12}	2.95×10^{12}	2.57×10^{11}	1.56×10^{10}
m_si	2.75×10^{-8}	9.26×10^{-8}	1.06×10^{-6}	1.75×10^{-5}
m_a		0.00000076		
m_s		0.00001872		